Journal of Global Positioning Systems (2025)

Vol. 21, Issue 1: 44-64

DOI:10.5081/jgps.21.1.44

Enhanced Low-Cost GNSS RTK Positioning with an Adaptive Threshold

Yalong Wang[1], Yuting Gao[1]✉, Qingzhi Zhao[1],Shurong Xue[1], Bopeng Sun[1],Feng Zhou[2]

1 College of Geomatics, Xi’an University of Science and Technology, Xi’an 710054, China

2 College of Geomatics, Shandong University of Science And Technology, QingDao 266590, China

✉ The corresponding author: Yuting Gao, ygao@xust.edu.cn

Abstract: Fault detection and identification algorithm is essential to ensure the reliability of global navigation satellite systems (GNSS) systems for high-precision intelligent applications. Low-cost receivers always suffers from GNSS pseudorange gross-error detection and carrier-phase cycle-slip anomaly in complex environments, which would degrade positioning accuracy. To address these issues, this paper proposes an enhanced low-cost RTK precise-positioning algorithm with an adaptive strategy, designed to detect multiple pseudorange gross errors and carrier-phase cycle slips. By leveraging time differenced darrier phase (TDCP) observations, the proposed method dynamically adjusts detection thresholds in real time, thereby minoring multiple faults and improving positining accuracy. To evaluate the performance of the proposed algorithm, a dynamic vehicle experiment equipped with ublox and BeiYun low-cost GNSS devices was conducted. Four schemes including GL, GLF, GLFTC, and GLFTA methods are compared. Results show that the 3D RMS positioning errors of the proposed GLFTA method achieves maximum 19.34% improvement. That is because the proposed GLFTA method incorporating an adaptive strategy can detect small carrier phase cycle slips than the GL, GLF, and GLFTC methods, thereby enhancing RTK positioning performance in complex environments.

Keywords: Global navigation satellite system (GNSS); Real-time kinematic (RTK); Time difference carrier phase(TDCP)

1.Introduction

Owing to the advantages of cost-effectiveness, high accuracy and rapid convergence, low-cost real time kinematic (RTK) positioning has a wide applications, such as UAV aerial navigation, autonomous intelligent transportation and so on. However, in complex environments, the GNSS observations inevitably contained multiple pseudorange faults and frequent cycle slips, which affected by multipath effects, signal interference, or satellite malfunctions. As a result, it would degrade the quality of GNSS observations and positioning accuracy.

Extensive research has been conducted to deal with this issue, mainly summarized with two approached including the detection of pseudorange faults and the detection of cycle slip in carrier phase observations. There are mainly two approaches to deal with pseudorange faults including fault detection and exclusion and robust estimation algorithms. For example, Jiang et al. proposed an enhanced advanced integrity monitoring extrapolation (AIME) method, which identifies faulty satellites by analyzing the innovation sequence and its covariance derived from a sliding-window Kalman Filter (KF)[1]. However, this approach relies heavily on a fixed-length window analysis of KF innovations, which may lead to missed detections or false alarms under dynamic environment. Alternatively, Du et al. proposed an proposed an advanced receiver autonomous integrity monitoring (ARAIM) fault detection and exclusion

Editor-In-Charge: Dr. Baocheng Zhang

(FDE) availability optimization method based on dynamic budget allocation. By dynamically distributing integrity and continuity risk budgets and adjusting the risk weights of different fault modes in real time, the method enhances the system availability and reliability under multi fault scenarios[2]. Liu et al.[3] proposed an FDE consistency check method based on virtual satellite pseudorange observations generated from an orbital database. By comparing the synthesized virtual measurements with real-time observations, the method effectively detects and excludes potential faults in the observation data. Wu et al. developed a least squares system innovation based FDE algorithm that avoids solving observation equations for all potential fault cases. Simulation results validated its performance and analyzed the influence of satellite geometry on detection effectiveness. However, they rely heavily on accurate stochastic modeling and exhibit limited capability in detecting correlated faults among multiple satellites. Furthermore, robust algorithms is another effective approach for achieving integrated Positioning, Navigation, and Timing (PNT) solutions[5]. Firstly, “Danish Method”, as the first application of robust estimation theory in surveying, has been introduced by Krarup et al.[6] in 1980. This method uses an iterative weight reduction strategy, though the weighting parameters are determined rather than through theoretical optimization. In addition, IGG (Institute of Geodesy and Geophysics) robust estimation[7] and IGG II model[8] have been proposed, which is based on equivalent weights and further improves the robustness of parameter initialization. On this basis, Yang[9] further proposed the IGG III robust estimation, later refined and extended in subsepuent studites[10]. Building on this foundation, Yang et al.[11]developed a series of robust adaptive filtering frameworks, including variance component estimation based robust adaptive filtering method[12]. At present, robust estimation algorithms can satisfy the demands of dynamic positioning and demonstrate robustness and computational efficicency. However, the robust estimation and FDE still have limited performance to detect multiple faults with constant threshold in complex environments.

Furthermore, cycle slips in carrier phase observations remains an essential issue in GNSS pre-processing[13]. For single frequency cycle slip detection, common approaches include the high-order difference method[14], polynomial fitting[15], and wavelet analysis[16-17]. For Dual frequency cycle slip detection, there are pseudorange/phase combination approach[18], TurboEdit[19] and STPIR (Satellite Time Phase Ionospheric System Innovation) algorithm[20]. Besides, geometry free and ionosphere free models are typically combined for triple frequency cycle slip detection[21]. In the single frequency cycle slip detection mode, Remondi first proposed the high order difference method, which laid the foundation for subsequent developments in cycle slip detection.This method applies successive epoch to epoch differencing to carrier phase observations, amplifying the impact of cycle slips and enabling accurate estimation of their magnitudes[22]. Beutler et al.[23] employed a polynomial fitting approach to detect cycle slips with a polynomial model, which is flexibile and adaptable through parameter adjustments but has poor real time performance. While the high-order difference method is sensitive to large cycle slips but amplifies observation noise, resulting in less effective for small cycle slips. Moreover, higher order polynomials may misinterpret random noise cycle slips, causing false detections. Blewitt[24] Proposed TurboEdit algorithm by forming the Melbourne Wübbena (MW) and Geometry Free (GF) combinations, and this algorithm is the most widely applied for cycle slips detection. However, the MW combination performs poorly for low elevation satellites, while the GF combination is highly sensitive to data sampling rates. To address these issue, Zhang et al.[25] analyzed large scale GNSS datasets and proposed an empirical threshold model to improve detection reliability. Overall, the TurboEdit algorithm has advantages of computational simplicity and minimized detection blind zones but remains sensitive to ionospheric variations[26]and less effective in identifying small cycle slips[27]. Thanks to TDCP method, known for its high sensitivity to small cycle slips[28][29], are combined with GF models for cycle slip detection.

For example, Xu et al.[30] proposed an effective GF+GB hybrid approach, where GF firstly detect large cycle slips and TDCP assisted to detect small cycle slip. Li et al.[31] proposed an enhanced Improved Geometry Free (IGF) integrated with the TDCP, enabling identification of small cycle slips on specific frequencies. In a novel study, Chen et al.[32]incorporated cycle slip processing into a TDCP GNSS/INS system by modeling cycle slips as outliers and mitigating them using a robust extended kalman filter (EKF). Similarly, Can et al.[33]employed raw GNSS observations to construct multiple linear combinations for cycle slip detection and repair, while employing posterior residuals from observation equations to identify additional outliers and slips. However, it still lacks a universally applicable solution for frequent small cycle slips across arbitrary frequencies. Overall, research on cycle slip detection has been more extensive for single frequency[34-37] and dual frequency[38-41] applications. Additionally, inertial navigation system (INS) data have been increasingly usd to assist in cycle slip detection[42-45].

Although extensive research has been conducted on fault detection in GNSS positioning systems, subatantial challenges presist in hangding pseudorange faults and frequent cycle slips in low cost GNSS devices. Existing methods struggle to promptly detect multiple faults, especially under complex conditions involving frequent small anomalies. Traditional detection techniques, which rely on empirically fixed thresholds, often fail to adapt to the multi fault characteristics of low cost GNSS receivers, resulting in degraded positioning accuracy. To address these limitations, this study proposes an enhanced RTK positioning method for low cost GNSS receivers. In pseudorange fault detection, the method integrates position-domain global detection with observation-domain local detection and combines fixed thresholds with sliding-window dynamic thresholds to effectively reduce missed detections under multiple gross error conditions. For carrier-phase processing, an adaptive threshold algorithm is developed to dynamically adjust detection limits based on the statistical characteristics of the observations, enabling accurate identification of frequent minor cycle slips.It is implemented within a low cost dynamic RTK framework and validated through vehicle mounted experiments. Experiment results show that the proposed method significantly improves RTK positioning performance by effectively detecting frequent minor faults while maintaining high precision in GNSS positioning.

2.Methodology

In this section, the methodology of the system innovation-based chi-square detection method and the doppler assisted TDCP observation for cycle slip detection would be introduced.

2.1 System Innovation based chi-square detection method

The system innovation based chi-square detection method is applied to effectively identify multiple pseudorange errors by integrating global and individual fault detection. When no fault is present, the linearized form of the GNSS observation equation at epoch k can be expressed as follows:

$$Z_k = H_k X_k + \Delta_k \tag{1}$$

Among these terms, Z_k denotes the observation vector, H_k represents the state geometry matrix, X_k refers to the state vector containing the unknown parameters, and Δ_k denotes the measurement noise vector, which is assumed to be temporally uncorrelated.

When a fault occurs, the fault model is denoted as ∇_k, and the linearized GNSS observation equation can be expressed as follows:

$$Z_k = H_k X_k + C_k \nabla_k + \Delta_k \tag{2}$$

The standard Kalman filter model forms the mathematical foundation for the system innovation based chi-square detection method. It primarily operates on the state and observation equations to generate the system innovation sequence, after which the chi-square test is applied to detect observation errors. The linear discrete system model of the standard Kalman filter can be described as follows:

$$\begin{cases} X_k = \boldsymbol{\Phi}_{k,k-1} X_{k-1} + \boldsymbol{\Gamma}_{k,k-1} W_{k-1} \\ Z_k = H_k X_k + \Delta_k \end{cases} \tag{3}$$

Here, X_k denotes the state vector, $\Phi_{k,k-1}$ represents the state transition matrix, $\Gamma_{k,k-1}$ is the control or coefficient matrix, Z_k stands for the measurement vector, and H_k corresponds to the measurement model coefficient matrix. The process noise vector W_k is typically modeled as zero-mean Gaussian white noise with covariance matrices Q_k and R_k, respectively, and W_k is assumed to be statistically independent of Δ_k.

The subsequent prediction step of the Kalman filter can be expressed as follows:

$$\bar{X}_{k,k-1} = \Phi_{k,k-1} \hat{X}_{k-1} \tag{4}$$

The system innovation vector can be expressed as follows:

$$V_k = Z_k - H_k \bar{X}_{k/k-1} \tag{5}$$

The covariance matrix of the system innovation vector can be expressed as follows:

$$P_{vk} = H_k P_{k,k-1} H_k^T + R_k \tag{6}$$

When no fault is present, the system innovation vector V_k behaves as zero-mean white noise. However, once a fault occurs, the statistical characteristics of the system innovation change, and its mean deviates from zero.

Therefore, two hypotheses are defined: the null hypothesis H_0 and the alternative hypothesis H_1. The null hypothesis H_0 indicates that no fault exists, which can be expressed as follows:

$$H_0 : E\{Z_k\} = H_k X_k \qquad V_k \sim N(0, P_{vk}) \tag{7}$$

Here, $D\{Z_k\} = Q_Z$ denotes the variance–covariance matrix of the observations, while $E\{\}$ and $D\{\}$ represent the expectation and dispersion factors, respectively. The alternative hypothesis H_1 indicates that a fault exists, which can be expressed as follows:

$$H_1 : E\{Z_k\} = H_k X_k + C_k \nabla_k\,, \quad V_k \sim (\mu,\ P_{vk}) \tag{8}$$

Here, C_k contains the observed values associated with the fault, and μ represents the mean of the system innovation vector V_k. Since fault detection requires redundant observations, it is assumed that m observations contain df degrees of freedom; therefore, the maximum number of detectable faults is $1 \le qm \le df$.

For fault detection and identification, the position estimation $(\hat{x}_0)$ is recalculated by deriving the updated position $(\hat{x}_i)$ from all observation domains, during which the suspicious observation faults in each fault mode are identified and removed. The fault detection and identification process is implemented through a two-step detection scheme that applies dual thresholds to accomplish both fault detection and identification. Accordingly, the global fault detection function can be expressed as follows:

$$\Lambda_k = V_k^T P_{vk}^{-1} V_k \tag{9}$$

The global detection statistic Λ_k follows the chi-square distribution function χ^2, whose degree of freedom df corresponds to the dimension of the observation vector. When no fault occurs, $\Lambda_k \sim \chi^2(0, df)$ obeys a central chi-square distribution, whereas in the presence of a fault, $\Lambda_k \sim \chi^2(\sigma, df)$ follows a non-central chi-square distribution characterized by the non-centrality parameter σ. Therefore, the global fault detection standard can be expressed as follows:

$$\begin{cases} \Lambda_k > T_{d1}, & \text{the existence of fault} \\ \Lambda_k < T_{d1}, & \text{no fault occurs} \end{cases} \tag{10}$$

Among them, T_{d1} represents the global monitoring threshold, which is determined based on the Neyman–Pearson criterion. When the false alarm rate is specified as α, the threshold T_{d1} can be obtained by solving the equation $P\{\Lambda_k > T_{d1} / H_0\} = \alpha$, through which the missed detection rate is minimized.

By calculating the global detection statistics and corresponding thresholds, the system can effectively perform global fault detection. This process is essential for identifying reliable observations, eliminating erroneous measurements, and incorporate local testing methods, thereby enhancing fault detection performance and improving the accuracy of RTK navigation solutions.

When a fault is identified through global detection at epoch k, the potential faults occurring at the same epoch are subsequently examined one by one. At this stage, the system innovation vector becomes $\bar{v}_k$, and the single-fault detection function can be expressed as follows:

$$\lambda_k^i = \frac{\left|\bar{v}_k^i\right|}{\sqrt{P_{vk}^{ii}}} \tag{11}$$

where λ_k^i denotes the normalized system innovation, P_{vk}^{ii} represents the ith diagonal element of the covariance matrix P_{vk}, and $\bar{v}_k^i$ corresponds to the ith element in v_k. When the observation vector contains a single fault, the null hypothesis is defined as $H_0 : \lambda_k^i \sim (0,1)$, whereas the alternative hypothesis is $H_1 : \lambda_k^i \sim (\delta_i, 1)$, where δ_i is a non-centrality parameter that can be determined according to the false alarm rate α_0 and the missed detection rate β_0. Therefore, the local fault detection criterion can be expressed as follows:

$$\begin{cases} \lambda_k^i > T_{d2}, & \text{the existence of fault} \\ \lambda_k^i < T_{d2}, & \text{no fault occurs} \end{cases} \tag{12}$$

Here, T_{d2} denotes the threshold used to detect the occurrence of a single fault, and its corresponding value, obtained from the Gaussian distribution function, is expressed as $N_{\alpha_0/2}(0,1)$.

During the fault detection process, each observation vector is individually tested for potential faults, as any measurement may be unreliable. Once both global and single fault detections are completed, the identified faulty measurements are removed, and the remaining valid observations are used to update the filter. This procedure iteratively performs local and single fault detection until the detection statistics meet the global threshold criterion.

2.2 Doppler assisted TDCP cycle slip detection

The dopper assisted TDCP cycle slip method can detecte carrier phase cycle slips with adaptive thresholds.The TDCP measurement is primarily based on the time differencing of carrier phases. It determines the relative position by evaluating the carrier phase time difference between two receivers or between a receiver and multiple satellites. The TDCP measurement represents the carrier phase change between two consecutive epochs, t_{k-1} and t_k, which can be expressed as follows:

$$\Delta\Phi = \Phi_{t_k} - \Phi_{t_{k-1}} = \frac{1}{\lambda}\Delta r + \frac{c}{\lambda}\Delta dt_R + \Delta N + \Delta\varepsilon_\Phi \tag{13}$$

In the above equation, $\Delta\Phi$ denotes the variation in the carrier phase measurement between two consecutive epochs, with the unit of cycles. Δr represents the change in the geometric distance between the receiver and the satellite, with the unit of meters. The symbol c denotes the speed of light in a vacuum. Δdt_R corresponds to the variation in receiver clock bias over time, while ΔN denotes the change in the carrier phase integer ambiguity. When no cycle slip occurs, ΔN remains zero. The term $\Delta\varepsilon_\Phi$ represents other unmodeled errors, which are typically small and therefore negligible.The change in the distance between the receiver and the satellite over two consecutive epochs can be expressed as:

$$\Delta r = r_{t_k} - r_{t_{k-1}} = \vec{r}_{t_k} \cdot (\Delta \mathrm{r}^s - \Delta \mathrm{r}^R) \tag{14}$$

wherein $\Delta \mathrm{r}^s$ and $\Delta \mathrm{r}^R$ denote the position increments of the satellite and the receiver, respectively, in the Earth-centered Earth-fixed coordinate system between two consecutive epochs. $\vec{r}_{t_k}$ represents the unit vector directed from the receiver to the satellite, while "·" denotes the vector inner product operator. Based on Eqs. (13) and (14), the expression for $\Delta\Phi$ can be written as follows:

$$\Delta\Phi = \frac{1}{\lambda}\vec{r}_{t_{k+1}} \cdot (\Delta r^s - \Delta r^R) + \frac{c}{\lambda}\Delta dt_R + \Delta N + \Delta\varepsilon_\Phi \tag{15}$$

Among them, $\Delta \mathrm{r}^R$ and Δdt_R are the unknown quantities, while all other variables can be determined except ΔN. The unknown parameters are estimated using the Least Squares Method (LSM), which can be formulated as follows:

$$\begin{bmatrix} \Delta r^R \\ c\Delta dt_R \end{bmatrix} = (B^T B)^{-1} B^T C \tag{16}$$

with $B=\begin{bmatrix}\vec{r}^{\,1}_{t_{k+1}} & -1\\ \vec{r}^{\,2}_{t_{k+1}} & -1\\ \vdots & \vdots\\ \vec{r}^{\,i}_{t_{k+1}} & -1\end{bmatrix}$, $C=\begin{bmatrix}\vec{r}^{\,1}_{t_{k+1}}\cdot\Delta r^{S1}-\lambda\Delta\Phi^{1}\\ \vec{r}^{\,2}_{t_{k+1}}\cdot\Delta r^{S2}-\lambda\Delta\Phi^{2}\\ \vdots\\ \vec{r}^{\,i}_{t_{k+1}}\cdot\Delta r^{Si}-\lambda\Delta\Phi^{i}\end{bmatrix}$.

In the actual positioning solution, the presence of ΔN may cause pronounced peaks to appear in the solution results. Therefore, efficient and accurate fault detection and identification plays a crucial role in ensuring an accurate and reliable TDCP solution.

For each satellite calculated using TDCP, the carrier phase integer ambiguity may vary between epochs. Since the doppler frequency shift is unaffected by cycle slips, the relationship between the doppler frequency shift and the carrier phase can therefore be established. The doppler integral, obtained by integrating the doppler shift over time, represents the total relative displacement of the receiver with respect to the satellite during an epoch interval. The carrier phase measurement can be interpreted as the doppler integral plus an unknown integer ambiguity. Unless the carrier tracking loop loses lock or experiences a phase discontinuity, the TDCP and the doppler integral remain consistent between the two epochs, indicating that no fault occurs. Consequently, TDCP is utilized to assist in fault detection and identification. The doppler integral difference between epochs t_k and t_{k+1} can be expressed as follows:

$$\mathrm{d}\Phi=-\int_{t_k}^{t_{k+1}}D\,dt \tag{17}$$

wherein D denotes the doppler frequency shift. Therefore, according to the relationship with TDCP, the difference between TDCP and $\mathrm{d}\Phi$ can be expressed as :

$$V=\Delta\Phi-\mathrm{d}\Phi=\Delta\Phi+\int_{t_k}^{t_{k+1}}D\,dt=\Delta\mathrm{N}+\varepsilon \tag{18}$$

Eq. (18) can be simplified into :

$$V=\Delta\Phi+\left(\mathrm{D}_{t_{k+1}}+D_{t_k}\right)\left(\mathrm{D}_{t_{k+1}}-D_{t_k}\right)/2=\Delta\Phi+\varepsilon \tag{19}$$

wherein $\mathrm{D}_{t_{k+1}}$ and D_{t_k} represent the doppler frequency shift measurements at epochs t_{k+1} and t_k, respectively, and $dt=t_{k+1}-t_k$ denotes the sampling interval. The remaining error, which is typically on the order of a few centimeters, is much smaller than a cycle slip represented by the symbol ε and can therefore be neglected. Consequently, the mathematical expectation and covariance of V can be expressed as follows:

$$\mathrm{E}(V)=\Delta N+\mathrm{E}(\varepsilon) \tag{20}$$

$$Cov(V)=Cov(\varepsilon) \tag{21}$$

wherein $E(V)$ denotes the mathematical expectation, $Cov(V)$ represents the covariance, and $E(\varepsilon)$ and $Cov(\varepsilon)$ correspond to the mathematical expectation and covariance within less than one cycle, respectively. Unlike traditional approaches, this method employs a real-time recursive computation to determine the test statistics and corresponding thresholds, thereby improving both the detection statistic and the threshold estimation. This enables rapid fault detection, precise fault identification and elimination, and the realization of an efficient and accurate multi-fault monitoring model, which ultimately enhances the quality of navigation observation data and the accuracy of subsequent integrity monitoring. Accordingly, the mean $\overline{\mathrm{V}}_k$ and variance σ^2_{k} of the current epoch V, calculated based on real-time recursive computation, can be expressed as follows:

$$\overline{\mathrm{V}}_k=\overline{\mathrm{V}}_{k-1}+\frac{1}{k}(\mathrm{V}_k-\mathrm{V}_{k-1}) \tag{22}$$

$$\sigma^2_k=\frac{k-2}{k-1}\sigma^2_{k-1}+\frac{1}{k}(\mathrm{V}_k-\overline{\mathrm{V}}_{k\text{-}1})^2 \tag{23}$$

wherein $\overline{\mathrm{V}}_k$ represents the mean value from epoch 1 to k, $\overline{\mathrm{V}}_{k-1}$ denotes the mean of V from epoch 1 to k -1, σ^2_k is the covariance matrix of V at epoch k, and $\sigma^2_{k\text{-}1}$ indicates the covariance matrix of V at epoch k -1. Accordingly, the test statistic and corresponding threshold for TDCP fault detection and identification can be expressed as follows:

$$\left|V_k-\overline{V}_k\right|\le m\cdot\sigma_k \tag{24}$$

wherein m denotes the scaling factor of the threshold, which determines the fault detection capability. As a fixed parameter, it is set to 3 according to the 3σ rule. If (24) is satisfied, a fault is considered to be present; otherwise, no fault is detected.

3 Data collection and processing

To verify the proposed method, a dynamic short-baseline experiment is conducted in Qujiang Cultural Park, Xi’an, Shaanxi Province, China. As shown in Figure 1, the reference station was established on the rooftop of the administrative building at the YanTa Campus of Xi’an University of Science and Technology. The reference station is equipped with Trimble BD990 receiver in an open-sky environment. As for the rover station depicted in Figure 2, u-blox F9P receiver modules and BeiYun M22 navigation boards were equipped on a moving vehicle. The experimental environment was relatively complex with several multipath effects. The experimental setup and operating environment for the rover are depicted in Figure 2.

The dynamic vehicle experiment covered a baseline of approximately 6.3 km, which rover data over 2,400 seconds. Both the reference station and the rover stations sampled at 1 Hz, recording pseudorange, carrier phase, and doppler measurements from four satellite constellations: GPS, BDS, Galileo, and GLONASS. Detailed dataset information is provided in Table 1.The reference trajectory was generated using the built in RTK solution of the commercial u-blox F9P receiver. During data collection, observations from the Trimble BD990 reference station were transmitted to the rover’s u-blox F9P module for internal RTK processing. According to the manufacturer, the F9P is built in RTK achieves an accuracy of about 10 mm + 1 ppm horizontal and 20 mm + 1 ppm vertical, sufficient to server as a reliable ground truth reference.The experiment equipment configuration is shown in Figure 3, and Figure 4 presents the sky plots of the observed BDS, GPS, GLONASS, and Galileo constellations observed during the test.

Figure 1. Configuration of the reference station and its surrounding environment

Figure 2. Data acquisition setup for the dynamic, vehicle mounted rover system

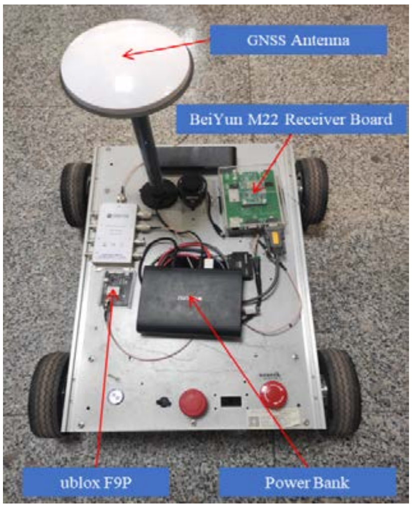

Figure 3. Equipment layout diagram for the dynamic vehicle-mounted experiment

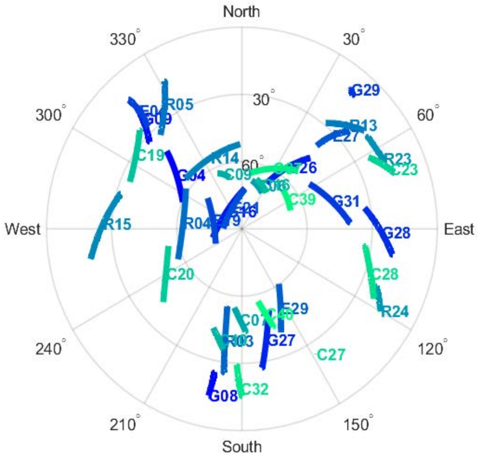

Figure 4. Sky plot of satellite visibility during the experiment.

Table 1. Description of the dynamic experiment dataset collection

Base equipment	Trimble BD990	
Rover equipment	u-blox F9P、BeiYun M22	
Sampling rate	1 Hz	
Elevation cut-off angle	10 degrees	
Observations	Pseudorange+carrier phase+doppler	
Elapsed time	2400s	
Baseline length	6.3 kilometers	
Acquired signals	GPS	C1C L1C D1C /C2S L2S D2S
	BDS	C2I L2I D2I/C5P L5P D5P
	GLONASS	C1C L1C D1C/C2C L2C D2C
	Galileo	C1B L1B D1B/C5P L5P D5P

Figure 5 trajectory of the vehicle experiment. The left panel shows the detailed route, including the start point and end points, while the right panel overlays the trajectory on a satellite map for clearer visualization.

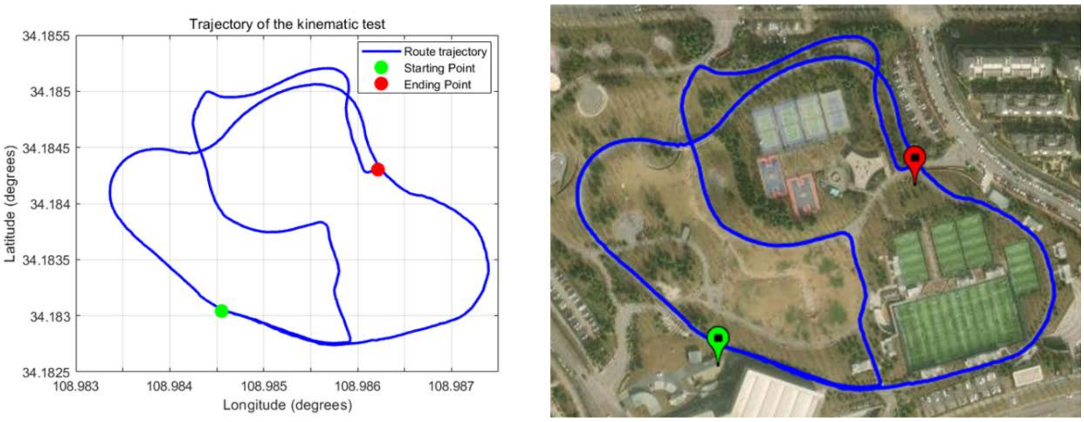

Figure 5. Trajectory of the dynamic moving-car test route

4 Experiments and results

In this section, we present a comprehensive analysis of data quality and experimental results. First, he observation quality from the BeiYun M22 and u-blox F9P datasets is evaluated. Then, the positioning performance and fault detection capabilities of four methods GL, GLF, GLFTC, and GLFTA are compared. The processing strategies of these methods are summarized in Table 2.

Table 2. Four schemes with different processing strategies

Scheme	Full name with different processing strategy
GL	GF+LLI method
GLF	GF+LLI+FDE method
GLFTC	GF+LLI+FDE+TDCP+ constant threshold
GLFTA	GF+LLI+FDE+TDCP +adaptive threshold

4.1 Experiment data analysis

To assess data quality, three key metrics were analyzed for the BeiYun M22 and u-blox F9P datasets: the number of visible satellites, carrier phase to pseudorange ratio, and the carrier phase cycle slip count, the results are shown in Figures 6 and 7. The carrier phase to pseudorange ratio indicates the proportiona of valid carrier phase to pseudorange observations; a higher ratio suggests less signal blockage and greater positioning stability. In contrast, the carrier phase cycle slip count reflects measurement continuity, as excessive slips often arise from receiver instability or poor signal propagation conditions, leading to reduced positioning accuracy. Notably, a lower carrier phase to pseudorange ratio accompanied by frequent cycle slips indicates degraded carrier phase continuity and consequently poorerl positioning performance.

Comparative analysis reveals notable distinctions between the two datasets. The BeiYun M22 receiver achieves an average carrier phase to pseudorange ratio of 98.4%, while the u-blox F9P records 83.1%. In terms of cycle slip frequency, BeiYun M22 average of 0.98% per epoch compared with 2.0% for u-blox F9P, indicating more stable carrier phase tracking for the former. Variations in visible satellite count directly affect the carrier phase to pseudorange ratio, as differences in satellite observation quality affects the proportional of uasble carrier phase and pseudorange measurements. Consequently, these variations determine the share of high quality data available for precise GNSS positioning.Figure 8 compares the HDOP, VDOP, and PDOP values for BeiYun M22 (left) and u-blox F9P (right). Both datasets maintain PDOP values below 1.0, indicating excellent satellite geometry. However, the u-blox F9P shows slightly better spatial distribution, providing improved observation stability and superior vertical(VDOP) performance. Overall, both receives meet the high precision positioning criterion(PDOP < 2).

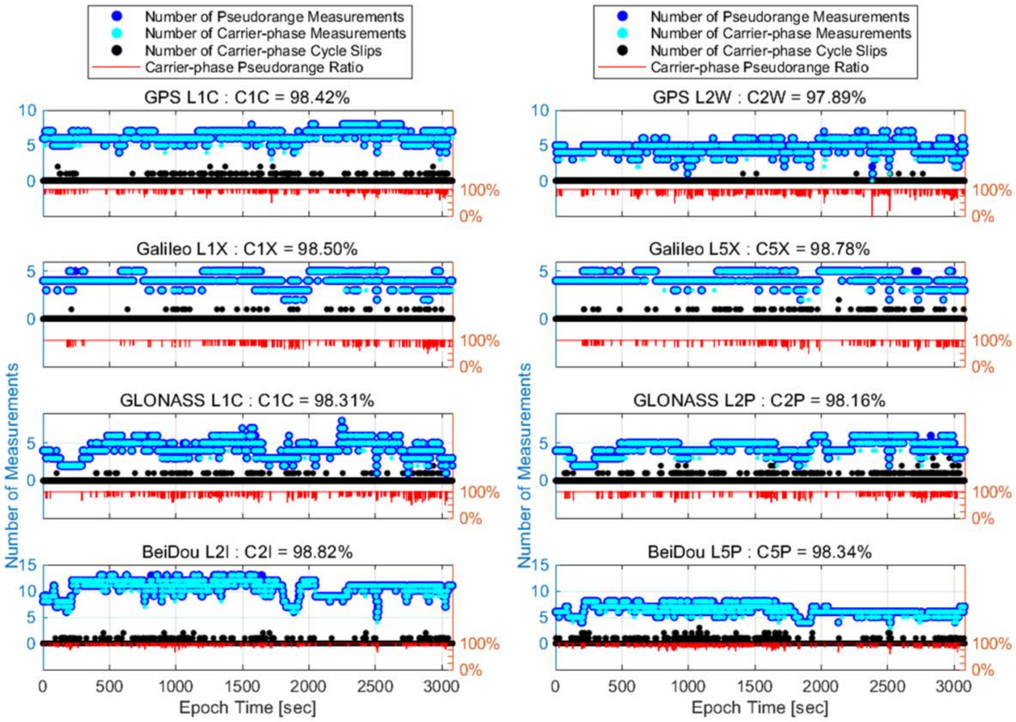

Figure 6. Number of BDS, GPS, GLONASS, and Galileo satellites, and their carrier phase to pseudorange ratios for the BeiYun M22 receiver.

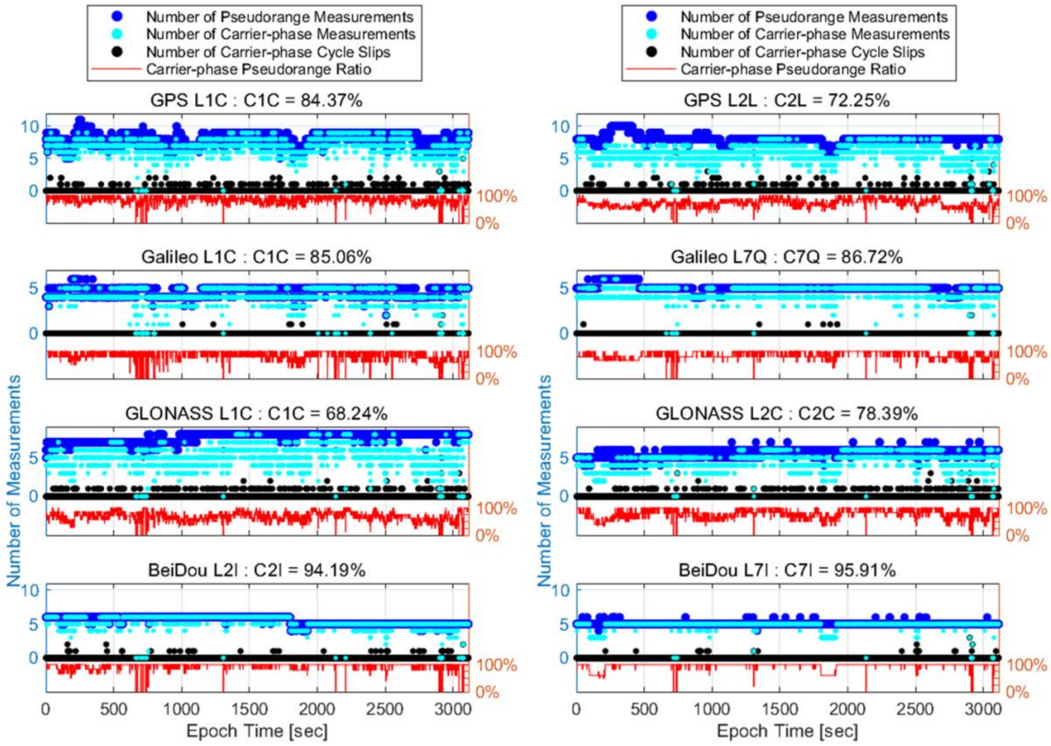

Figure 7. Number of BDS, GPS, GLONASS, and Galileo satellites, and their carrier-phase–to-pseudorange ratios for the u-blox F9P receiver.

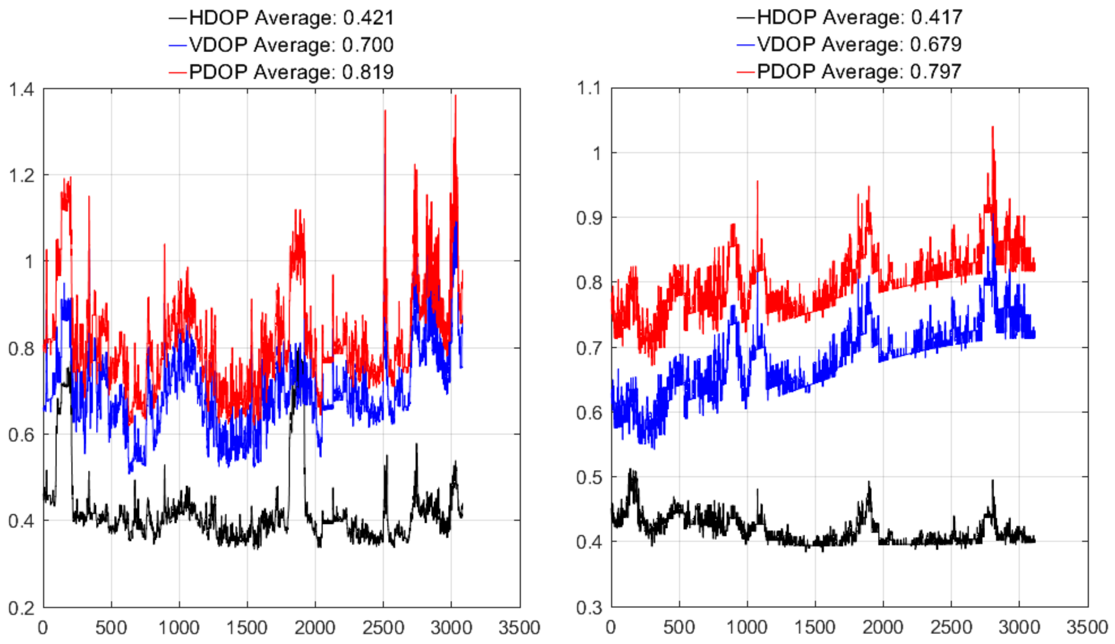

Figure 8. HDOP, VDOP, and PDOP values for the BeiYun M22 dataset (left) and the u-blox F9P dataset (right).

4.2 Experiment result analysis

This section systematically evaluates the performance of the four methods GL, GLF, GLFTC, and GLFTA in terms of cycle slip detection and positioning accuracy. The analysis focuses on comparing detection performance and analyzing RTK positioning accuracy. A dynamic vehicle experiment was conducted to collect multi constellation GNSS data in complex environments, enabling verification of algorithm robustness. In addition, rigorous statistical analysis were performed to quantify differences among the four methods, providing a solid basis for evaluating their effectiveness under realistic conditions.

4.2.1 Comparison of cycle slip detection anomalies

This section compares the cycle-slip detection performance of four methods GL, GLF, GLFTC, and GLFTA using data from the BeiYun M22 and u-blox F9P receivers. Figure 9 shows the cycle slip distribution for BeiYun M22 (left) and u-blox F9P (right), where the horizontal axis represents observation epochs and the vertical axis idicates satellite numbers. Different colors and markers are used to distinguish the four methods. As shown in Figure 9, the GLFTA method detects the largest number of cycle slips for BeiYun M22, including all slips identified by the GL, GLF, and GLFTC methods, as well as additional ones missed by the others. This demonstrates its high detection sensitivity, particularly for small or short duration cycle slips. Tthe detected cycle slips are relatively continuous and spatially clustered, mainly due to sudden environmental changes during the dynamic vehicle experiment.For the u-blox F9P dataset, the GLFTA method once again detects the most cycle slips, encompassing all detections from the other three methods. Compared with BeiYun M22, u-blox F9P exhibits a greater number and denser distribution of cycle slips, primarily due to the hardware limitations of low cost receivers, which tintroduce higher observation noise.To further highlight performance differences among the four methods, line charts of detected cycle slips counts for both datasets were generated for clearer quantitative comparison.

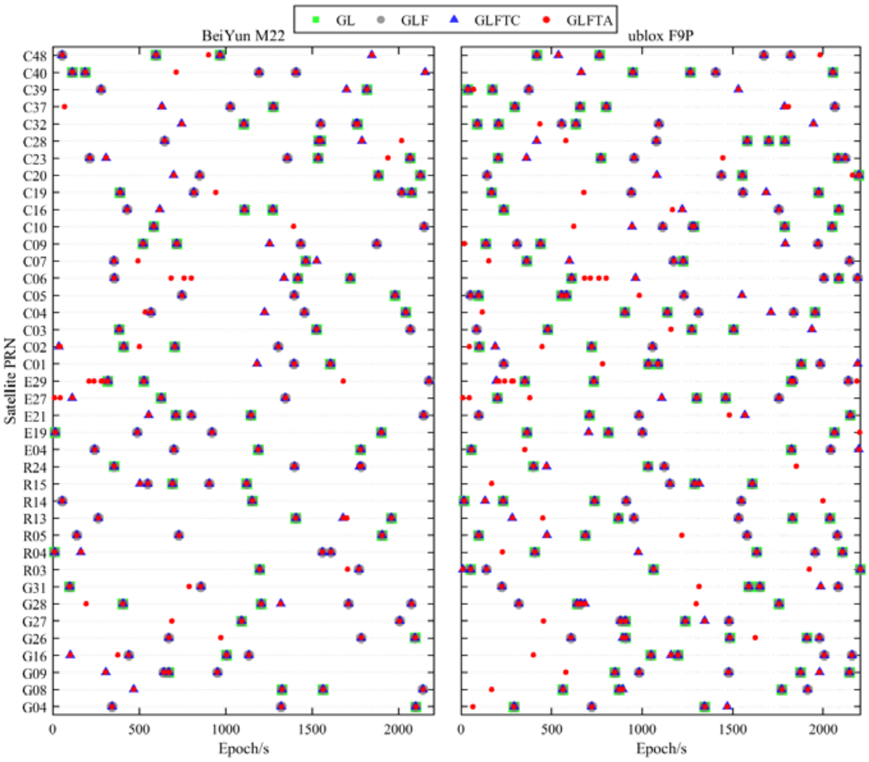

Figure 9. Cycle-slip detection distributions obtained using four methods (GL, GLF, GLFTC, and GLFTA) for the BeiYun M22 dataset (left) and the u-blox F9P dataset (right).

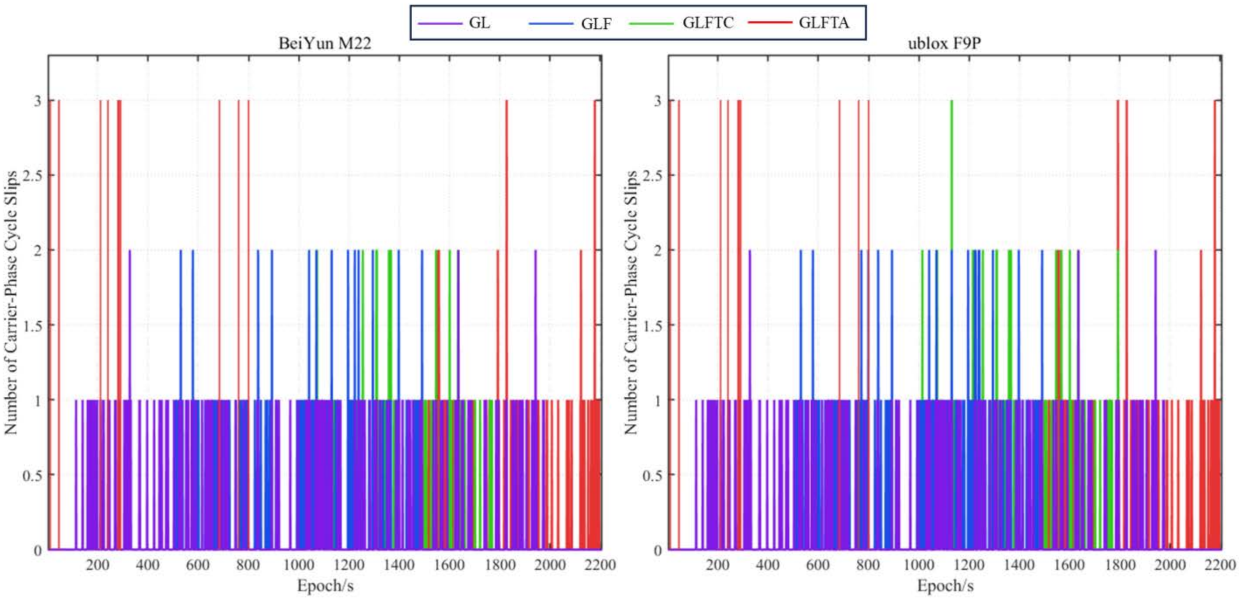

Figure 10. Line charts comparing the number of detected cycle slips using four methods (GL, GLF, GLFTC, and GLFTA) for the BeiYun M22 dataset (left) and the u-blox F9P dataset (right).

As shown in Figure 10, the cycle slip detection distributions across epochs for the BeiYun M22 and u-blox F9P datasets were compared using the four methods GL, GLF, GLFTC, and GLFTA.For the BeiYun M22 dataset, the GLFTA method, shown in red and positioned at the bottom layer, detected the largest number of cycle slips. It successfully identified all cycle slips captured by the GL, GLF, and GLFTC methods, including all epochs with triple cycle slips, demonstrating a comprehensive detection capability. For the u-blox F9P dataset, the GLFTA method again achieved the highest detection count. Compared with BeiYun M22, u-blox F9P exhibited more frequent and concentrated cycle slips, particularly around epoch 1200.

To further validate the performance of the adaptive dynamic threshold in carrier phase cycle slip detection, statistical analyses of detection thresholds and test statistics were conducted using the BeiYun M22 dataset. Six representative satellites E27, E29, C02, C06, R14, and R15 were selected for evaluation. Figure 11 illustrated the distribution of the adaptive dynamic thresholds and corresponding test statistics. As shown, several epochs exhibited test statistics exceeding their thresholds, confirming successful cycle slip detection. The adaptive thresholds adjusted dynamically with varying observation conditions, maintaining sensitivity to subtle changes in signal quality. For satellites C02 and C06, most detected cycle slips occurred around epoch 44 and 660-800, where noticeable variations between thresholds and test statistics were observed. Similarly, satellites E27 and E29 showed significant slip events, with E29 exhibiting higher frequency between epochs 200-300. Table 4 summarizes the comparison between the fixed-threshold and adaptive dynamic-threshold methods for the six satellites. The results demonstrate that the adaptive dynamic threshold method is more sensitive in detecting minor or short-duration cycle slips and achieves superior positioning accuracy by effectively identifying these subtle anomalies.

Table 4 presents the statistical results of cycle slips detected by the GLFTC and GLFTA methods. The results show that, compared with the fixed threshold GLFTC method, the proposed adaptive threshold GLFTA approach detects a greater number of cycle slips, demonstrating significantly improved fault detection capability. Furthermore, the GLFA method successfully identifies small cycle slips missed by the GLFC method and maintains effective detection performance across all satellites.

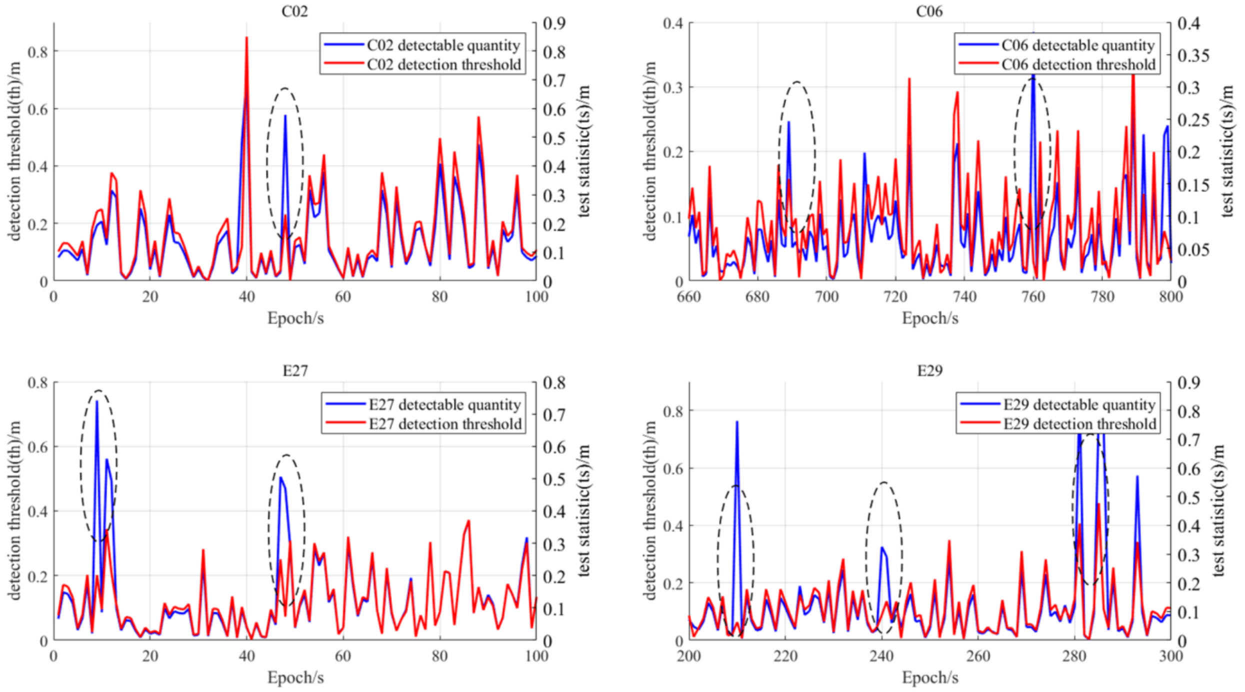

Figure 11. Distribution of cycle-slip detection thresholds and test statistics for each satellite based on the adaptive dynamic threshold method.

Table 4. Statistical comparison of cycle-slip detection counts between the adaptive dynamic threshold method and the fixed threshold method across satellites (unit: epoch).

Abbreviation	Satellite ID					
	C02	C06	E27	E29	R14	R15
GLFTC	7	15	15	11	18	11
GLFTA	16	19	22	23	27	18

4.2.2 Positioning results analysis and comparison

To further assess the RTK positioning accuracy of the four methods, a comparative analysis was conducted across all experimental schemes. Figure 12 shows the positioning errors in the East, North, and Upward directions for both the BeiYun M22 (left) and u-blox F9P datasets, using the GL, GLF, GLFTC, and GLFTA methods. The BeiYun M22 results show that the GL (green) and GLF (black) methods yield similar error across all three directions. In contrast, the GLFTC (blue) method shows notable improvements in accuracy, while the GLFTA (red) method achieves the highest overall precision. Notably, the GL and GLF methods exhibit errors during the first 50 epochs, with significant error jumps around the 100th epoch and between epochs 1000-1500. In contrast both GLFTC and GLFTA methods perform better across all directions, especially in reducing initial fluctuations and eliminating error jumps near the 100th epoch. The GLFTA method consistently outperforms GLFTC, especially during the first 50 epochs and around epoch 1000, confirming the effectiveness and adaptability of the proposed adaptive threshold strategy in improving positioning stability and accuracy under dynamic conditions.

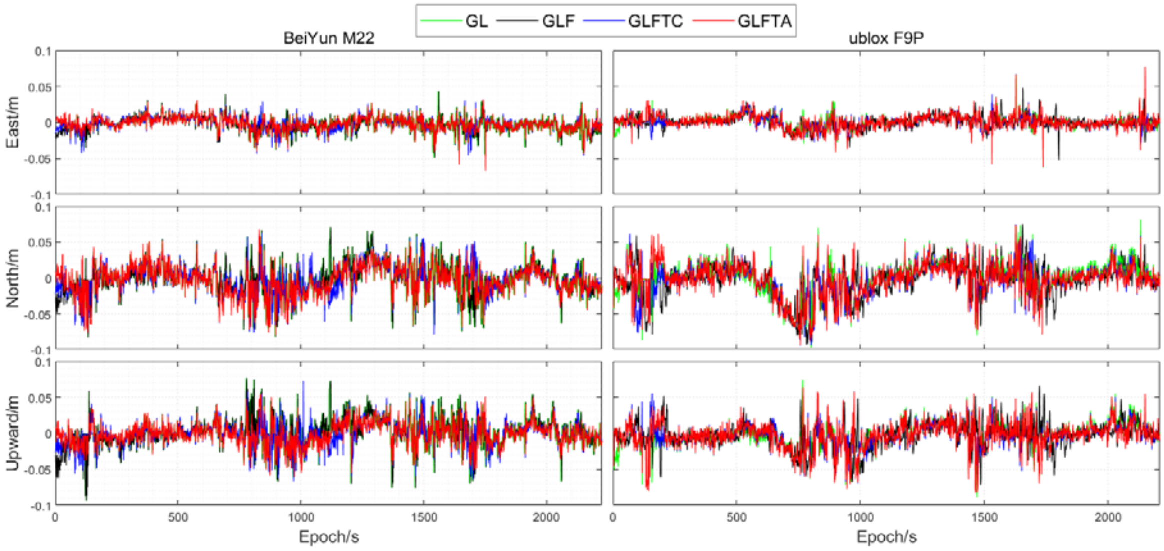

Figure 12. Comparison of positioning errors in the East, North, and Up directions among the four methods (GL, GLF, GLFTC, and GLFTA) for the BeiYun M22 dataset (left) and the u-blox F9P dataset (right).

The positioning error plot for the u-blox F9P dataset clearly shows that the GL (green) and GLF (black) methods produce the largest errors across all three coordinate components. In contrast, the GLFTC (blue) and GLFTA (red) methods demonstrate significantly better performance. Notably, the GL and GLF methods exhibit much larger errors during the first 50 epochs, with distinct error jumps around the 100th epoch and between epochs 1000-1500. In comparison, the GLFTC and GLFTA methods show considerable improvements in accuracy, effectively reducing initial fluctuations and eliminating errors near the 100th epoch. The GLFTA method further outperforms GLFTC, particularly in the first 50 epochs and around epoch 1000, highlighting its superior adaptability under dynamic signal conditions. Between epochs 50 and 2100, both GLFTC and GLFTA maintain significantly lower errors than GL and GLF, demonstrating their better stability and robustness. Overall, the GLFTA method resolves issus where GL and GLF, and even GLFTC under fixed threshold conditions, fail to achieve reliable convergence, achieving better accuracy in all coordinate directions. The adaptive threshold mechanism of GLFTA enhances fault detection sensitivity, further improving positioning accuracy.

Table 5. RMS, STD, and improvement rate statistics for the BeiYun M22 dataset (unit: meters).

Scheme		GL	GLF	GLFTC	GLFTA
RMS	East	0.0192	0.0179	0.0136	0.0134
	North	0.0297	0.0291	0.0257	0.0246
	Upward	0.0234	0.0204	0.0200	0.0196
STD	East	0.0279	0.0178	0.0136	0.0134
	North	0.0290	0.0289	0.0254	0.0242
	Upward	0.0232	0.0203	0.0197	0.0191
3D RMS		0.0424	0.0398	0.0353	0.0342
Improvement Percentage		0	6.13%	16.75%	19.34%

Table 6. RMS, STD, and improvement rate statistics for the u-blox F9P dataset (unit: meters).

Scheme		GL	GLF	GLFTC	GLFTA
RMS	East	0.0223	0.0192	0.0181	0.0164
	North	0.0298	0.0279	0.0263	0.0251
	Upward	0.0245	0.0234	0.0222	0.0204
STD	East	0.0219	0.0186	0.0176	0.0160
	North	0.0296	0.0275	0.0261	0.0250
	Upward	0.0245	0.0232	0.0222	0.0203
3D RMS		0.0446	0.0412	0.0390	0.0363
Improvement Percentage		0	7.62%	12.56%	18.61%

Tables 5 and 6 summarize the positioning errors statistics for the BeiYun M22 and u-blox F9P datasets, comparing the performance of the methods GL, GLF, GLFTC, and GLFTA methods in terms of RMS, STD, and percentage improvement across the East, North, Upward, and 3D directions.For Table 5, the 3D RMS for the GL method is 0.0424 m, while the GLF method improve this to 0.0398 m, representing a 6.13% imorovement in the 3D direction. The GLFTC method further reduces the 3D RMS to 0.0353 m， showing a 16.75% improvement over the GL method. The GLFTA method achieves the best performance with a 3D RMS of 0.0342 m, reflecting a 19.34% improvement over the GL method. From Table 6, The 3D RMS values for the GL, GLF, GLFTC, and GLFTA methods are 0.0446, 0.0412, 0.0390, and 0.0363, respectively. The GLF method shows a 7.62% improvement over GL in the 3D direction, the GLFTC method improves by 12.56%, and the GLFTA method achieves an 18.61% improvement compared to GL. The statistical results from Tables 5 and 6 clearly indicate that, compared to the traditional GL method, the other three methods consistently deliver better positioning accuracy, with the dynamic adaptive threshold method GLFTA demonstrating the most significant improvements.

Figure 13 presents the comparative bar charts of RMS values in the East, North, Upward, and 3D directions for the four methods GL, GLF, GLFTC, and GLFTA using the BeiYun M22 and u-blox F9P datasets. The chart clearly shows a gradual reduction in RMS values from GL to GLFTA, indicating progressively improved positioning performance. Notably, the GLFTA method demonstrates the most significant RMS reduction compared to the GL method, achieving the lowest RMS in all directions, while the GL method consistently exhibits the highest RMS values across all directions.

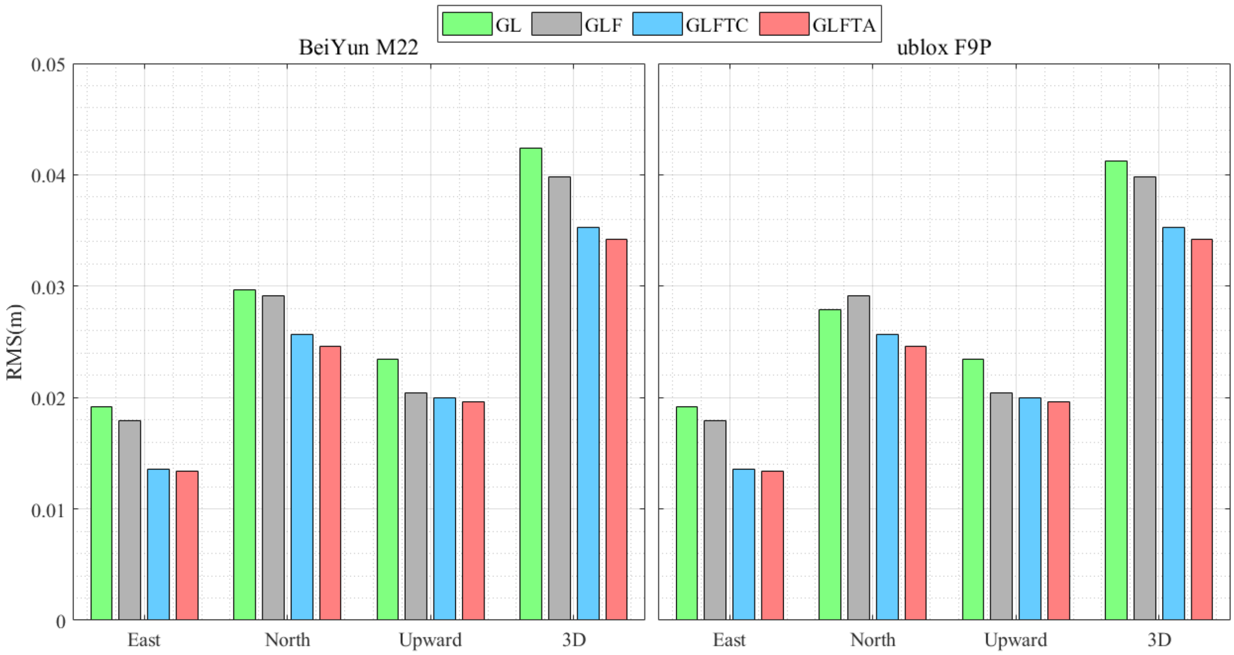

Figure 13. Comparative bar charts of RMS values in the East, North, Up, and 3D directions for the BeiYun M22 (left) and u-blox F9P (right) receivers using the four methods (GL, GLF, GLFTC, and GLFTA).

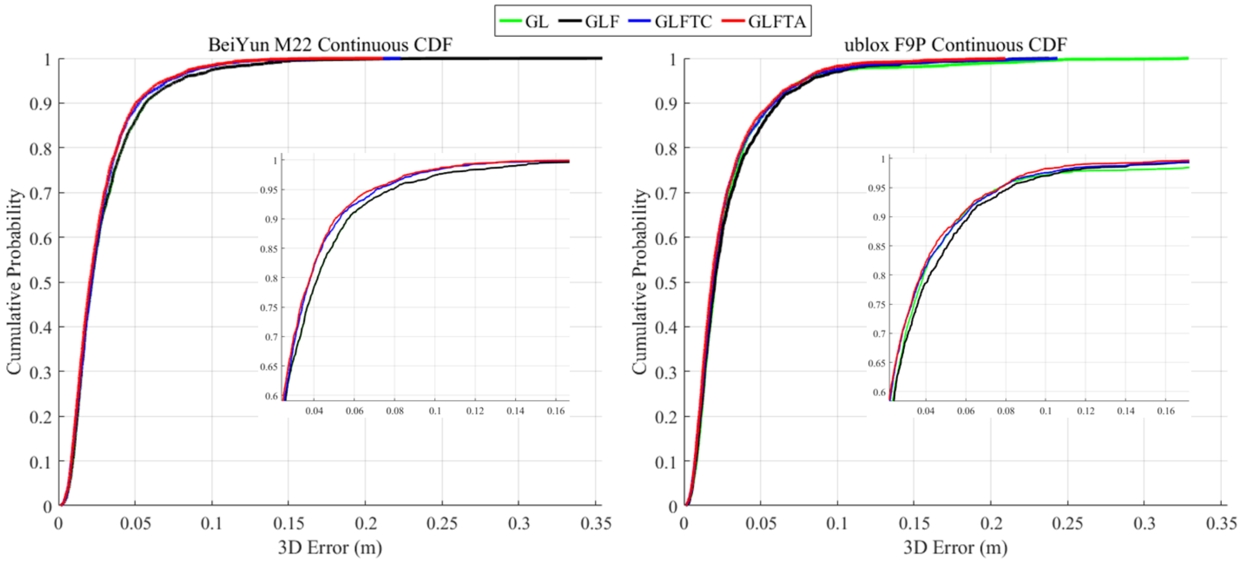

Figure 14. Cumulative distribution statistics of positioning errors for the BeiYun M22 (left) and u-blox F9P (right) receivers.

To provide a clearer comparison of positioning performance between the BeiYun M22 and u-blox F9P datasets, Figure 14 presents the cumulative distribution function CDF statistics of 3D positioning errors for the four methods GL, GLF, GLFTC, and GLFTA with BeiYun M22 on the left and u-blox F9P on the right. The horizontal axis represents error magnitude, while the vertical axis indicates the probability of the error not being exceeded. The shape and steepness of the CDF curves reflect the accuracy distribution and reliability of each method.

From Figure 14, the green GL and black GLF curves exhibit nearly identical CDF characteristics with only minor variations, both showing gentle ascents and relatively low slopes in the error >0.15 m region. Approximately 50% of their positioning errors fall within ≤0.025 m, while the error tails extend beyond 0.3 m, indicating limited stability and sensitivity to multipath interference or signal obstructions. In contrast, the blue GLFTC curve demonstrates intermediate steepness, achieving notable improvement in the low error region (≤0.025 m) compared with GL and GLF, yet retaining a moderate tail length, suggesting partial suppression of large outliers. The red GLFTA curve, however, displays the steepest ascent and most compact distribution, rapidly increasing within the low error range, where 50% of the positioning errors are ≤0.02 m. Its tail segment is considerably shorter and flatter, signifying enhanced stability and concentration of errors. When zooming into the regions with rapid CDF growth, these distinctions become even more apparent across both datasets. Overall, the CDF analysis confirms that the GLFTA adaptive algorithm effectively adjusts detection thresholds in real time, effectively, suppressing outlier errors and enhancing positioning robustness. This mechanism results in more concentrated error distributions, greater reliability, and markedly improved positioning consistency compared with the other three methods.

5 Summary and conclusions

To address multiple pseudorange gross errors and carrier phase cycle slips in low cost GNSS receivers, this study proposes an enhanced RTK method incorporating an adaptive dynamic threshold adjustment mechanism for dynamic RTK positioning. This approach effectively reduces missed detections of pseudorange errors, enables timely identification of minor cycle slips, and significantly enhances positioning accuracy and reliability. Validation using dynamic vehicle experiments confirms that the proposed method can detect additional cycle slips and substantially improve RTK performance for low-cost GNSS devices under complex environments. Conclusions are summarized as follows:

(1) The analysis of data quality evaluation shows that the high end BeiYun M22 receiver maintained a carrier phase to pseudorange observation ratio of 98.4%, compared with 83.1% for the low cost ublox F9P. The average cycle slip occurrence rate was 0.98% per epoch for BeiYun M22 and 2.0% for ublox F9P. These discrepancies can be attributed to hardware design and environmental influences, indicating that the low-cost ublox F9P is inherently more susceptible to cycle slips.

(2) The proposed adaptive GLFTA method can effectively detect cycle slips that were miss-detected by the GL, GLF, and GLFTC approaches. Results demonstrate that dynamic threshold-based strategies offer significant advantages for GNSS fault detection under complex and time-varying conditions.

(3) It illustrated that the GLFTC with fixed-threshold and GLFTA with adaptive threshold methods reduced the 3D RMS of positioning errors by 16.75% and 19.34% for BeiYun M22, and by 12.56% and 18.61% for ublox F9P, when compared to the GL method. Particularly, the GLFTA method based on the low cost ublox F9P datasets shows the most improvement, underscoring its capability to enhance positioning accuracy even on cost-optimized hardware.

Acknowledgement: The financial support was provided by the National Natural Science Foundation of China (42204034), the Xi'an Association for Science and Technology Young Talent Fund (959202313075).

References

[1] Jiang, H., Yan, D., Wang, J., Yin, J. (2024). Innovation-based Kalman filter fault detection and exclusion method against all-source faults for tightly coupled GNSS/INS/Vision integration. GPS solutions, 28(3), 108.

[2] Du, J., Fang, K., Wang, Z., Zhu, Y. (2024). Availability evaluation and optimisation of advanced receiver autonomous integrity monitoring fault detection and exclusion considering temporal correlations. IET Radar, Sonar & Navigation, 18(10), 1966-1979.

[3] Liu, J., Zhao, X. (2020). GNSS fault detection and exclusion based on virtual pseudorange-based consistency check method. Chinese Journal of Electronics, 29(1), 41-48.

[4] Wu, Q. A. (2024). A two-fault detection and elimination approach to the receiver autonomous integrity monitoring. GPS Solutions, 28(4), 160.

[5] Q., Liu, J., Jiang, J., Pang, X., Ge, Z. (2025). Application of improved fault detection and robust adaptive algorithm in GNSS/INS integrated navigation. Remote Sensing, 17(5), 804.

[6] Krarup, T. (1980). Götterdämmerung over least squares adjustment. In Proceedings of the 14th Congress of the International Society of Photogrammetry (Vol. 3, pp. 369–378).

[7] Zhou, J. (1989). Classical theory of errors and robust estimation. Acta Geodetica et Cartographica Sinica, 18, 115-120.

[8] Zhou, J., Wang, Y., (1992) Robust fitting estimation [C] // Collection of robust estimation papers [M].Beijing : Surveying and Mapping Press : 41-50.

[9] Yuanxi, Y. A. N. G. (1994). Robust estimation for dependent observations. Manuscripta geodaetica, 19(1), 10-17.

[10] Yang, Y., Song, L., Xu, T. (2002). Robust estimator for correlated observations based on bifactor equivalent weights. Journal of geodesy, 76(6), 353-358.

[11] Yang, Y., He, H., Xu, G. (2001). Adaptively robust filtering for kinematic geodetic positioning. Journal of geodesy, 75(2), 109-116.

[12] Yang, Y., Xu, T. (2003). An adaptive Kalman filter based on sage windowing weights and variance components. The journal of Navigation, 56(2), 231-240.

[13] Xu, S., Zhang, H., Yang, Z., (2003) GPS measurement principle and application [M].Wuhan : Wuhan University Press.

[14] Kleusberg, A., Peyton, D., Wells, D. (1990, March). Airborne gravimetry and the global positioning system. In IEEE Symposium on Position Location and Navigation. A Decade of Excellence in the Navigation Sciences (pp. 273-278). IEEE.

[15] Lichtenegger, H., Hofmann Wellenhof, B. (1990). GPS-data preprocessing for cycle-slip detection. In Global Positioning System: An Overview: Symposium No. 102 Edinburgh, Scotland, August 7–8, 1989 (pp. 57-68). New York, NY: Springer New York.

[16] Westrop, J., Napier, M. E., Ashkenazi, V. (1989). Cycle slips on the move: detection and elimination. In Proceedings of the 2nd International Technical Meeting of the Satellite Division of The Institute of Navigation (ION GPS 1989) (pp. 31-34).

[17] Collin, F., Warnant, R. (1995). Application of the wavelet transform for GPS cycle slip correction and comparison with Kalman filter. Manuscripta Geodaetica, 20(3), 161-172.

[18] Han, S. (1997). Ambiguity recovery for long-range GPS kinematic positioning. Navigation, 44(2), 257-266.

[19] Blewitt, G. (1990). An automatic editing algorithm for GPS data. Geophysical research letters, 17(3), 199-202.

[20] Cai, C., Liu, Z., Xia, P., Dai, W. (2013). Cycle slip detection and repair for undifferenced GPS observations under high ionospheric activity. GPS solutions, 17(2), 247-260.

[21] Cai S., Zeng., (2021) Doppler integral reconstruction and STPIR combined cycle slip detection and repair [J]. Journal of Surveying and Mapping, 2021,50 (02) : 160-168.

[22] Remondi, B. W. (1985). Performing centimeters relative surveying in seconds using GPS Carrier Phase [J]. J Inst Navig, 32(4), 386-400.

[23] Beutler, G., Davidson, D. A., Langley, R. B., Santerre, R., Vaníček, P., Wells, D. E. (1984). Some theoretical and practical aspects of geodetic positioning using carrier phase difference observations of GPS (Global Positioning System) satellites. Mitteilungen Satell.-Beobachtungsstn. Zimmerwald, 14.

[24] Blewitt, G. (1990). An automatic editing algorithm for GPS data. Geophysical research letters, 17(3), 199-202.

[25] Zhang, Guo., Li., (2012) Real-time quality control in GNSS precise point positioning [J].Journal of Wuhan University (Information Science Edition), 37 (8) : 940-944.

[26] Banville, S., Langley, R. B. (2013). Mitigating the impact of ionospheric cycle slips in GNSS observations. Journal of Geodesy, 87(2), 179-193.

[27] Cai, C., Liu, Z., Xia, P., Dai, W. (2013). Cycle slip detection and repair for undifferenced GPS observations under high ionospheric activity. GPS solutions, 17(2), 247-260.

[28] Kirkko-Jaakkola, M., Traugott, J., Odijk, D., Collin, J., Sachs, G., Holzapfel, F. (2009, October). A RAIM approach to GNSS outlier and cycle slip detection using L1 carrier phase time-differences. In 2009 IEEE Workshop on Signal Processing Systems (pp. 273-278). IEEE.

[29] Zou, X., Li Z, Chen, L., (2017) A method for detecting and repairing single-frequency cycle slips between epochs [J].Journal of Wuhan University (Information Science Edition), 42 (10) : 1406-1410.

[30] Xu, T., Zhang, Z., He X,. (2023) A multi-cycle-slip detection and repair method for single-frequency GNSS data [J/OL].Journal of Wuhan University (Information Science Edition) : 1-17 [2023-11-17].

[31] Li, F., Gao, J., Zheng, N., Pan, C., Zhao, L. (2020). A novel dual-domain filtering method to improve GNSS performance based on a dynamic model constructed by TDCP. IEEE Access, 8, 79716-79723.

[32] Chen, K., Chang, G., Chen, C., Zhu, T. (2021). An improved TDCP-GNSS/INS integration scheme considering small cycle slip for low-cost land vehicular applications. Measurement

Science and Technology, 32(5), 055006.

[33] Cai, H., Zhao, Q., Sun, H., Hu, Z. (2011). GNSS real-time data quality control. Geomatics and Information Science of Wuhan University, 36(7), 820-824.

[34] Zangeneh-Nejad, F., Amiri-Simkooei, A. R., Sharifi, M. A., & Asgari, J. (2017). Cycle slip detection and repair of undifferenced single-frequency GPS carrier phase observations.Gps Solutions, 21(4), 1593-1603.

[35] Momoh, J. A., Bhattarai, S., Ziebart, M. (2019). Receiver clock jump and cycle slip correction algorithm for single-frequency GNSS receivers. GPS Solutions, 23(2), 38.

[36] Li, B., Liu, T., Nie, L., Qin, Y. (2019). Single-frequency GNSS cycle slip estimation with positional polynomial constraint. Journal of geodesy, 1-23.

[37] Zhao, J., Hernández-Pajares, M., Li, Z., Wang, L., Yuan, H. (2020). High-rate Doppler-aided cycle slip detection and repair method for low-cost single-frequency receivers. Gps solutions, 24(3), 80.

[38] Zhao, Q., Sun, B., Dai, Z., Hu, Z., Shi, C., Liu, J. (2015). Real-time detection and repair of cycle slips in triple-frequency GNSS measurements. GPS solutions, 19(3), 381-391.

[39] Ye, S., Liu, Y., Song, W., Lou, Y., Yi, W., Zhang, R., Xiang, Y. (2016). A cycle slip fixing method with GPS+ GLONASS observations in real-time kinematic PPP. GPS solutions, 20(1), 101-110.

[40] Ju, B., Gu, D., Chang, X., Herring, T. A., Duan, X., Wang, Z. (2017). Enhanced cycle slip detection method for dual-frequency BeiDou GEO carrier phase observations. Gps Solutions, 21(3), 1227-1238.

[41] Feng, W., Zhao, Y., Zhou, L., Huang, D., Hassan, A. (2020). Fast cycle slip determination for high-rate multi-GNSS RTK using modified geometry-free phase combination. Gps Solutions, 24(2), 42.

[42] Lee, H. K., Wang, J., Rizos, C. (2003). Effective cycle slip detection and identification for high precision GPS/INS integrated systems. The Journal of Navigation, 56(3), 475-486.

[43] Takasu, T., Yasuda, A. (2008, September). Cycle slip detection and fixing by MEMS-IMU/GPS integration for mobile environment RTK-GPS. In Proceedings of the 21st international technical meeting of the satellite division of the Institute of Navigation (ION GNSS 2008) (pp. 64-71).

[44] Du, S., Gao, Y. (2012). Inertial aided cycle slip detection and identification for integrated PPP GPS and INS. Sensors, 12(11), 14344-14362.

[45] Li, Z., Gao, J., Wang, J. (2016). Inertial aided cycle slip detection and repair for PPP/INS tightly coupled navigation. The Journal of Navigation, 69(6), 1357-1378.

Authors

Yalong Wang received the B.E. degree in Surveying Engineering from Liaoning University of Science and Technology, China, in 2022. He is currently pursuing the M.Sc. degree at Xi'an University of Science and Technology, Xi'an, China. His research focuses on GNSS/INS integrated navigation.

Yuting Gao (Member, IEEE) is a associate professor at the Xi’an University of Science and Technology. She received the Ph.D. degree in Geomatics Engineering at University of Calgary from 2017 to 2021. Her research focuses on integrity monitoring of GNSS precise positioning, low-cost GNSS receiver and non-Gaussian modeling.

Qingzhi Zhao received the B.Sc. degree from Shandong Agricultural University, Taian, China,in 2011,the M.Sc. degree from China University of Mining and Technology, Xuzhou, China,in 2014, and the Ph.D.degree from Wuhan University, Wuhan, China, in 2017.He is an Associate Professor with Xi'an University of Science and Technology, Xi'an, China.His research interests include Global Navigation Satellite System (GNSS) data processing and GNSS meteorology.

Shurong Xue is currently a master student at Xi'an University of Science and Technology. His current research focuses on GNSS/INS integrated navigation.

Bopeng Sun is currently a master student at Xi'an University of Science and Technology. His current research focuses on GNSS ambiguity resolution.

Feng Zhou is a associate professor at Shandong University of Science and Technology. He received the Ph.D. degree in East China Normal University from 2013 to 2018. His research focuses on: GNSS undifferenced and uncombined precise data processing theory and methods; regionally and widely-area integrated PPP-RTK fast real-time precise positioning technology; precise point positioning ambiguity resolution; multi-source sensor fusion theory and data processing.